

Request for funds for a high accuracy beam energy measurement system for BESIII

Submitted by the University of Hawaii
on Behalf of the BES Collaboration

F. A. Harris, Q. Liu, S. L. Olsen, C. P. Shen, G. S. Varner
Dept. of Physics and Astronomy,
University of Hawaii,
Honolulu, Hawaii 96822, U.S.A.

September 26, 2008

Abstract

The precise determination of the beam energy at BESIII is extremely important for many physics analyses, in particular, for the precise measurement of the τ mass. Fortunately, a method has been developed by physicists from the Budker Institute of Nuclear Physics (BINP) using back scattered Compton photons produced by CO_2 laser beams on both the electron and positron beams in BESIII. This method has been demonstrated at BESSY-I, BESSY-II, VEPP-4M, and VEPP-3 storage rings at Novosibirsk. The expected precision at BESIII is at the level of $\Delta\varepsilon = 40$ keV, or $\Delta\varepsilon/\varepsilon \approx 2 \cdot 10^{-5}$.

A collaboration has been formed between BINP, IHEP, and the University of Hawaii to install and commission such a system in BESIII. Hawaii will be responsible for the CO_2 laser and a power meter. All groups are responsible for contributing to the installation and commissioning. The total cost of the Hawaii proposal is \$119 K.

Contents

1	Introduction	4
2	Significance of the τ mass measurement	5
3	Status of m_τ	6
3.1	Threshold scan method	6
3.2	Decay kinematics method	8
4	Significance of beam energy measurement for a precise measurement of m_τ.	9
5	Significance of beam energy measurement for scan experiments	10
6	Significance for branching ratio determinations	11
7	New beam energy measurement technique	13
7.1	Compton Scattering	14
7.2	Beam energy measurement	15
7.3	Laser - electron luminosity	17
8	Energy measurement at BESIII	19
8.1	Laser source and power meter	20
8.2	Optics	22
8.3	Laser-to-vacuum insertion	24
8.4	Compton backscattering region	27
8.5	HPGe detector	30
9	Accuracy of the BEPC-II beam energy calibration system	32
9.1	Statistical Errors	32
9.1.1	The Compton Edge	32
9.1.2	The Energy Scale	33
9.2	Systematic Errors	33
9.2.1	Non-linearity of the HPGe energy scale	33
9.2.2	Other sources of systematic errors	33
10	Background measurements	33
11	Collaboration, budget, and schedule	37
12	Final budget	37

13 Summary

37

14 Acknowledgments

38

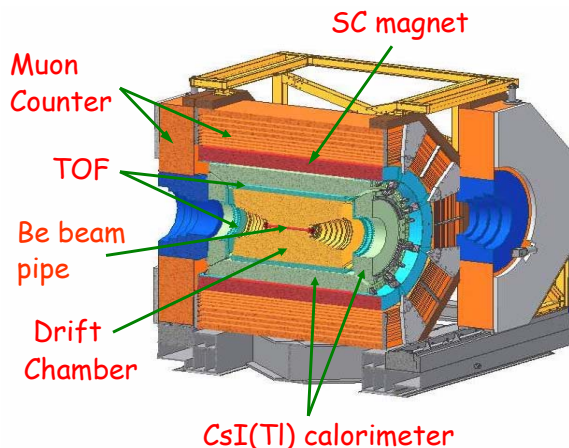


Figure 1: BESIII cut-away diagram.

1 Introduction

The Beijing Electron-Positron Collider (BEPC) and the Beijing Spectrometer (BES) [1, 2] have operated in the tau-charm center-of-mass energy region from 2 to 5 GeV since 1990. Now, BEPC has been upgraded to a two ring collider (BEPCII) [3], and BES has also been successfully upgraded to BESIII. Commissioning of BEPCII and BESIII together began in July, events have been obtained, and regular data taking will start this fall. The peak design luminosity of BEPCII is $10^{33} \text{ cm}^{-2} \text{ s}^{-1}$ ($1 \text{ nb}^{-1} \text{ s}^{-1}$) at 1.89 GeV, an improvement of a factor of 100 with respect to the BEPC, and is the highest luminosity ever planned in the τ -charm region [4].

Also, the detector performance is greatly improved compared to BESII [5]. BESIII, shown in Fig. 1, is a new detector and features a beryllium beam pipe; a small-cell, helium-based drift chamber (MDC); a Time-of-Flight (TOF) system; a CsI(Tl) electromagnetic calorimeter; a 1 Tesla superconducting solenoidal magnet; and a muon identifier using the magnet yoke interleaved with Resistive Plate Chambers.

With large cross sections in the tau-charm energy region, great numbers of events can be expected in the near future. With huge data samples together with excellent detector performance, unprecedented precision in this energy region can be expected in most physics analyses. To achieve such accurate measurements, systematic effects from many factors need to be seriously considered, among which is the beam energy.

The uncertainty of the beam energy is a crucial factor for many interesting and fundamental measurements, such as measurements of the τ mass and the determination of the $\psi(2S)$ resonance parameters. Here, we will describe a method to determine the beam energy to very high precision using back-scattered Compton photons, produced by scattering a laser beam from the e^+ or e^- beam.

2 Significance of the τ mass measurement

The τ lepton mass, m_τ , is one of the fundamental parameters of the Standard Model. The relationships between the τ lifetime, mass, and its leptonic branching fractions are simple and predicted by theory unambiguously. Therefore, the experimental determination of these parameters to the highest possible precision is essential. The measurements of e and μ masses have reached precisions of $\delta m/m$ of $\sim 10^{-8}$, while for τ , it is $\sim 10^{-4}$ [6].

A precise m_τ measurement is required to check lepton universality. In the standard model, all lepton doublets have identical charged-current couplings to the W boson. One can test this by comparing leptonic or semileptonic decays which only differ in lepton flavor. Figure 2 shows Feynman diagrams for $\tau \rightarrow e\nu_\tau\bar{\nu}_e$ and $\tau \rightarrow \mu\nu_\tau\bar{\nu}_\mu$, where the couplings, g , at each vertex are allowed to differ. If charged current universality holds, $g_e = g_\mu = g_\tau = g$. For example, using the electronic branching fractions of τ and μ , lepton universality can be tested as:

$$\left(\frac{g_\tau}{g_\mu}\right)^2 = \frac{\tau_\mu}{\tau_\tau} \left(\frac{m_\mu}{m_\tau}\right)^5 \frac{B(\tau \rightarrow e\nu\nu)}{B(\mu \rightarrow e\nu\nu)} (1 + \delta_W)(1 + \delta_\gamma). \quad (1)$$

where τ_l denotes a particle lifetime, B denotes a branching fraction, and δ_W and δ_γ are the weak and electromagnetic radiative corrections [7]. Note, the value of $(g_\tau/g_\mu)^2$ depends on m_τ to the fifth power.

The present situation is shown in Table 1 [8]. Present data verify the universality of leptonic charged current couplings to the 0.2% level [9].

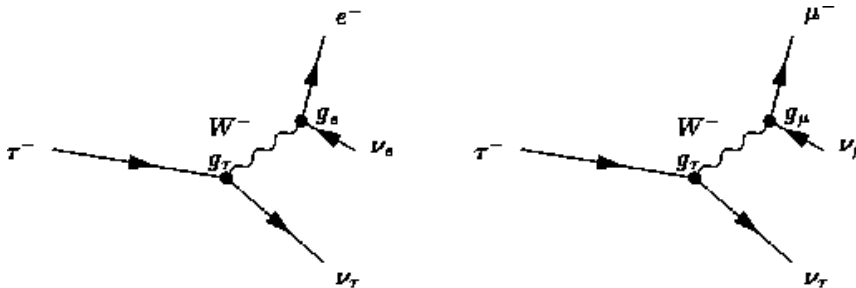


Figure 2: Feynman diagrams for $\tau \rightarrow \mu\nu_\tau\bar{\nu}_\mu$ and $\tau \rightarrow e\nu_\tau\bar{\nu}_e$.

The τ leptonic branching fractions and τ lifetime are known with a precision of 0.3% [9], but improved lifetimes can be expected from Belle and BaBar. Universality tests require also a good determination of m_τ^5 , which is only known to the 0.08% level [6]. BESIII offers the opportunity to improve the precision of m_τ and to help provide the most stringent tests of universality.

Table 1: Experimental determinations of $|g_l/g_{l'}|$ [8].

	$ g_\tau/g_\mu $
$\Gamma_{\tau \rightarrow e}/\Gamma_{\mu \rightarrow e}$	1.0006 ± 0.0022
$\Gamma_{\tau \rightarrow \pi}/\Gamma_{\pi \rightarrow \mu}$	0.996 ± 0.005
$\Gamma_{\tau \rightarrow K}/\Gamma_{K \rightarrow \mu}$	0.979 ± 0.017
$\Gamma_{W \rightarrow \tau}/\Gamma_{W \rightarrow \mu}$	1.039 ± 0.013
	$ g_\mu/g_e $
$\Gamma_{\tau \rightarrow \mu}/\Gamma_{\tau \rightarrow e}$	1.0000 ± 0.0020
$\Gamma_{\pi \rightarrow \mu}/\Gamma_{\pi \rightarrow e}$	1.0021 ± 0.0016
$\Gamma_{K \rightarrow \mu}/\Gamma_{K \rightarrow e}$	1.004 ± 0.007
$\Gamma_{K \rightarrow \pi\mu}/\Gamma_{K \rightarrow \pi e}$	1.0021 ± 0.0025
$\Gamma_{W \rightarrow \mu}/\Gamma_{W \rightarrow e}$	0.997 ± 0.010
	$ g_\tau/g_e $
$\Gamma_{\tau \rightarrow \mu}/\Gamma_{\mu \rightarrow e}$	1.0005 ± 0.0023
$\Gamma_{W \rightarrow \tau}/\Gamma_{W \rightarrow e}$	1.036 ± 0.014

The precision of m_τ will also restrict the ultimate sensitivity of m_{ν_τ} . The most sensitive bounds on the mass of the ν_τ can be derived from the analysis of the invariant mass spectrum of semi-hadronic τ decays, e.g. the present best limit of $m_{\nu_\tau} < 18.2 \text{ MeV}/c^2$ (95% CL) was based on the kinematics of 2939 $\tau^- \rightarrow 2\pi^- \pi^+ \nu_\tau$ and 52 $\tau^- \rightarrow 3\pi^- 2\pi^+ (\pi^-) \nu_\tau$ decays [10]. This method depends on a determination of the kinematic end point of the mass spectrum; thus high precision on m_τ is needed.

3 Status of m_τ

The world average of $m_\tau = 1776.99_{-0.26}^{+0.29} \text{ MeV}/c^2$ [6] is dominated by the BES collaboration measurement [11]. Figure 3 shows the measurements of the mass of the τ lepton. Recently the KEDR collaboration performed a threshold scan at the VEPP-4M collider [12], and the Belle collaboration has used the kinematics of hadronic tau decays to obtain the τ mass value with high statistics [13]. Considering these two new results, the updated value of m_τ is $1776.90 \pm 0.20 \text{ MeV}/c^2$ [14].

3.1 Threshold scan method

This method is based on the measurement of the $e^+e^- \rightarrow \tau^+\tau^-$ cross section in the region around threshold. The τ mass is derived from a fit to the cross section as a function of energy, which is described by the Standard Model. Here, a strategy can be

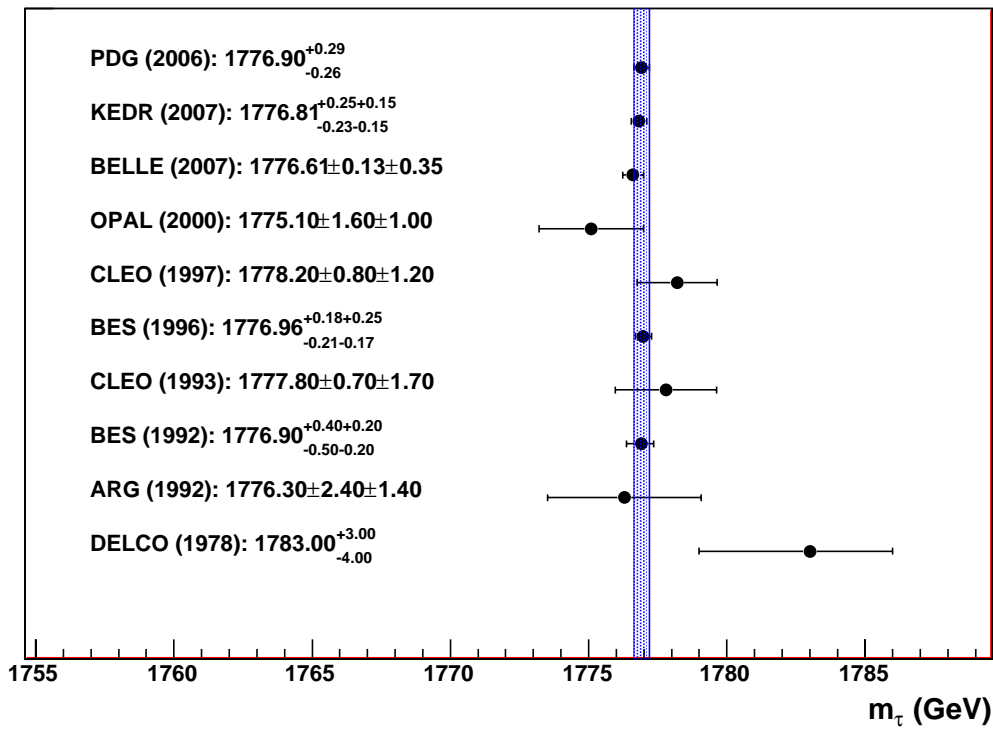


Figure 3: Values of m_τ obtained from experiments, compared to the 2006 world average of the Particle Data Group. The band indicates the current world average and error, $m_\tau = 1776.99^{+0.29}_{-0.26} \text{ MeV}/c^2$ [6].

used to choose energy points to obtain the maximum m_τ sensitivity for a given amount of luminosity. However, the disadvantages of this method are that the cross section and number of events are small near threshold and the beam energy must be known precisely.

The first accurate measurement of the τ mass was obtained by DELCO using this method in 1978, and it dominated the world average until 1992 [15]. Their energy scan, covering from 3.1 GeV to 7.4 GeV, allowed it to unambiguously conclude that the spin of τ is $1/2$. The DELCO result was $m_\tau = 1782_{-7}^{+2}$ MeV/ c^2 which was later refined to $m_\tau = 1783_{-4}^{+3}$ MeV/ c^2 after calibrating the energy scale using the measurement of the $\psi(2S)$ mass.

The BES measurement in 1996 was based on the combined data from the ee , $e\mu$, eh , $\mu\mu$, μh , and hh final states where h denotes a charged π or K [11]. The data were collected at twelve different energies within a range of 27 MeV around threshold, with an integrated luminosity of 5.07 pb^{-1} . Measurements of the J/ψ and $\psi(2S)$ peaks were also used to calibrate the beam energy scale. The result is $m_\tau = 1776.96_{-0.21-0.17}^{+0.18+0.25}$ MeV/ c^2 .

The KEDR collaboration measured m_τ in 2007 [12]. The beam energy was monitored using Compton backscattering of laser light, which is being proposed for BESIII. The accuracy of the beam energy measurement is better than 5×10^{-5} or 60 keV. With this energy measurement, the result is $m_\tau = 1776.96_{-0.23}^{+0.25} \pm 0.15$ MeV/ c^2 , based on 6.7 pb^{-1} of data which was collected at nine energy points around threshold.

3.2 Decay kinematics method

This method is based on the kinematics of hadronic τ decays, such as $\tau^- \rightarrow \pi^- \pi^- \pi^+ \nu_\tau$. The advantage of this method is a large sample can be obtained easily; thus the statistical error can be smaller. The disadvantage of this method is several assumptions must be made. Approximating the τ direction by the direction of the 3π particles, a pseudomass m_τ^* can be defined:

$$m_\tau^* = 2(E_\tau - E_{3\pi})(E_{3\pi} - p_{3\pi}) + m_{3\pi}^2. \quad (2)$$

where E_τ is the τ energy and $E_{3\pi}$, $p_{3\pi}$, and $m_{3\pi}$ are the energy, momentum, and mass of the three π system. This method was first applied by the ARGUS collaboration in 1992 [16]. They used a large sample of about 11000 τ events and obtained $m_\tau = 1776.3 \pm 2.4 \pm 1.4$ MeV/ c^2 .

The CLEO collaboration employed the same technique but applied it to hh events, such as $h\rho$, $\rho\rho$ events, in 1997 [17]. They obtained $m_\tau = 1776.3 \pm 0.8 \pm 1.2$ MeV/ c^2 . The OPAL collaboration fitted the τ pseudomass spectrum in $\tau^\pm \rightarrow \pi^\pm \pi^0 \nu_\tau$ and $\tau^\pm \rightarrow \pi^\pm \pi^+ \pi^- \pi^0 \nu_\tau$, and obtained $m_\tau = 1775.1 \pm 1.6 \pm 1.0$ MeV/ c^2 [18]. In 2007, m_τ was measured by Belle in the decay mode $\tau \rightarrow 3\pi \nu_\tau$ from 414 fb^{-1} of data [13]. The result is $m_\tau = 1776.61 \pm 0.13 \pm 0.35$ MeV/ c^2 .

4 Significance of beam energy measurement for a precise measurement of m_τ .

A Monte Carlo simulation has been employed to study the optimal data taking strategy for a new high precision m_τ measurement at BESIII [19]. From the results of Ref. [19], an empirical formula was obtained:

$$\delta m_\tau [\text{keV}/c^2] = \frac{708}{\mathcal{L}^{0.504}} \quad \text{or} \quad \frac{\delta m_\tau}{m_\tau} = \frac{3.98 \times 10^{-4}}{\mathcal{L}^{0.504}}, \quad (3)$$

where \mathcal{L} denotes the integrated luminosity (in units of pb^{-1}), δm_τ is the uncertainty in the fit to the threshold behavior. Based on Eq. (3), the necessary luminosity required for a certain precision can be readily obtained. For example, for $\delta m_\tau = 100 \text{ keV}/c^2$, then \mathcal{L} should be 49 pb^{-1} ; furthermore, for $\frac{\delta m_\tau}{m_\tau} = 1 \times 10^{-5}$, then \mathcal{L} must be at least 1500 pb^{-1} .

At BESIII, the design peak luminosity is around $1 \text{ nb}^{-1}\text{s}^{-1}$, and if the average luminosity is taken as 50% of the peak value, then two days of data taking will lead to a statistical uncertainty of m_τ less than $100 \text{ keV}/c^2$. Note this is solely for $e\mu$ -tagged events; if more channels are utilized to tag τ -pairs, such as ee , $e\mu$, eh , $\mu\mu$, μh , and hh ($h = \text{hadron}$), more statistics can be obtained. According to previous BES analyses [20, 21], the number of multi-channel-tagged events is at least five times more than that for $e\mu$ -tagged events alone. Therefore at BESIII, one week of data taking time will lead to a statistical uncertainty of less than $17 \text{ keV}/c^2$ for the m_τ measurement.

Table 2: Uncertainties for m_τ from assumed errors in various quantities. Note the Energy scale uncertainty is the absolute error, not the relative error. No assumed error is given for the theoretical accuracy, since the threshold region is fitted with two different models to determine this effect.

Source	assumed error (%)	δm_τ (keV/c^2)	$\delta m_\tau/m_\tau$ (10^{-6})
Luminosity	2.0	14.0	7.9
Efficiency	2.0	14.0	7.9
Branching Fraction	0.5	3.5	2.0
Background	10	1.7	1.0
Energy spread	30	3.0	1.7
Theoretical accuracy	–	3.0	1.7
Energy scale	0.1 MeV	100	56.3
Total		102	57.5

Also very important for a precision measurement are the systematic errors. For the run strategy studies, the following uncertainties on various experimental factors are assumed:

2% for the luminosity, \mathcal{L} ; 2% for the efficiency, ϵ ; 0.5% for the branching fraction, $B_{e\mu}$; 10% for the background, σ_{BG} ; and 30% for the energy spread. In addition, the uncertainty due to the theoretical calculation is obtained by comparing two formulas with different accuracies [22, 23, 24]. However, the most important source of uncertainty in the m_τ measurement is the precision on the absolute beam energy. For the m_τ measurement at BES I, this uncertainty was 0.1 MeV [25], and assuming it is the same at BES III, it will be the dominant uncertainty. The effects on the tau mass error due to the assumed uncertainties are summarized in Table 2. Clearly, the beam energy uncertainty is the bottleneck for the further improvement of the precision of m_τ .

5 Significance of beam energy measurement for scan experiments

Another important high energy physics experiment is a scan experiment, which provides fundamental information about a resonance, such as mass, total decay width, and partial decay widths. Very important at BES III will be scans of the $\psi(2S)$ and $\psi(3770)$, as well as a very detailed scan through the charm resonance region above the $\psi(3770)$ in order to shed light on some of the X, Y, Z particles [26]. Recently BES II found evidence for an anomalous line shape in $e^+e^- \rightarrow \text{hadrons}$ in the region of the $\psi(3770)$ [27], so a scan of this region will be high priority for BES III.

Moreover, some special analyses can only be done based on a scan experiment. For example, the phase between the strong and electromagnetic interaction can only be measured in a model independent way by a scan experiment [28, 29]. However, if the accuracy of the beam energy is poor, there will be a large uncertainty for the resonance mass. In fact, the beam energy uncertainty affects all fit parameters determined in a scan experiment.

As an example, we consider a scan in the vicinity of the ψ' . The following χ^2 estimator is used to obtain the resonance parameters

$$\chi^2 = \sum_{i=1}^{n_{pt}} \frac{(N_i - \mathcal{L}_i \cdot \epsilon_i \cdot \sigma(E_i, \vec{\eta}))^2}{(\Delta N_i)^2}, \quad (4)$$

where N_i (ΔN_i), \mathcal{L}_i , ϵ_i , $\sigma(E_i, \vec{\eta})$, and n_{pt} are the observed number of events (corresponding uncertainty), integrated luminosity, efficiency, observed cross section at each energy point E_i , and the total number of points taken for the scan experiment, respectively. The observed cross section depends on the energy at each point and on the resonance parameters (denoted by $\vec{\eta}$). The energy E_i is the value provided by the accelerator measurement system, but the actual energy may be shifted within the energy-measurement uncertainty, δE . We estimate the effects of such an uncertainty with the help of Monte Carlo simulation [30]. Specifically, for the assumed experiment, the energy E_i at each point is given

by:

$$E_i = E_i^0 + \xi_i , \quad (5)$$

where E_i^0 indicates the measured energy, ξ_i is a random number produced according to a Gaussian distribution with width δE . Here, we assume the energy uncertainty for all scan points is the same. With a given set of energy points and minimizing Eq. (4), we can obtain a group of fitting parameters ($\vec{\eta}$). Similarly, another sampling leads to another set of fitting parameters. We continue this process until we acquire distributions for each resonance parameter, and fitting the distributions, we get the corresponding errors. Figure 4 shows the effect of the energy uncertainty on the partial widths. It can be seen that the uncertainties of the partial widths increase almost linearly with the energy uncertainty. For example, the uncertainty in the partial width for $\psi(2S) \rightarrow \mu^+\mu^-$ is 1.7% for an energy uncertainty of 0.1 MeV. At BESIII because of the large statistics, the uncertainties due to other factors will become small, but without a better determination of the beam energy, the effect of the beam energy measurement will remain the same as for BESII. The effect due to accuracy of the energy measurement dominates, and the uncertainty of the measured value of the energy will determine the final accuracy of the the $\psi(2S)$ resonance widths.

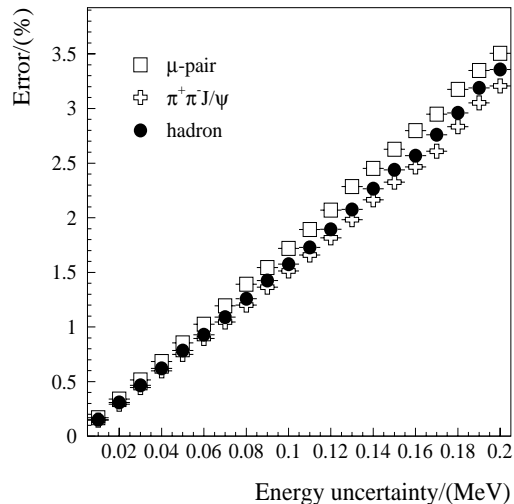


Figure 4: The effect of the energy uncertainty on the $\psi(2S)$ resonance partial widths.

6 Significance for branching ratio determinations

At an e^+e^- collider, the observed cross section near a resonance is complicated and depends sensitively on the beam energy, as well as other factors, including initial state radiation (ISR) and the beam energy spread. For example, the resonance height is reduced

and the position of its peak is shifted due to initial state radiation (ISR) and the energy spread of the collider. Moreover, in e^+e^- experiments, resonance production is accompanied by virtual photon continuum production, and there may be interference between the two processes [31, 32]. Such effects are especially important for narrow resonances like the J/ψ and $\psi(2S)$.

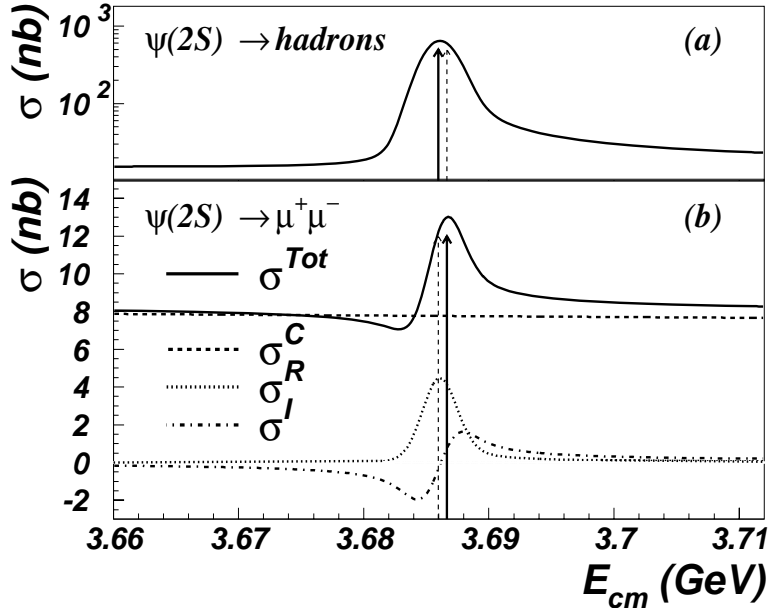


Figure 5: Cross sections in the vicinity of $\psi(2S)$ for (a) inclusive hadrons and (b) $\mu^+\mu^-$ final states. The solid arrow indicates the peak position and the dashed arrow the position of the other peak. In (b), the dashed line is QED continuum production (σ^C), the dotted line is resonance production (σ^R), the dash-dotted line is interference (σ^I), and the solid line is the total cross section (σ^{Tot}).

Figure 5 depicts the observed cross sections of inclusive hadrons (as a representative for hadronic decays) and μ -pairs (as a representative for electromagnetic decays) at the $\psi(2S)$. The two arrows in the figure denote the different positions of the maximum heights of the cross sections. The relative contribution of the resonance and the continuum varies rapidly as the energy changes. In actual experiments, data are naturally taken at the energy which yields the maximum inclusive hadronic cross section. This energy does not coincide with the maximum cross section of each exclusive mode. So it is important to know the beam spread and beam energy precisely in order to correctly subtract the continuum contribution and determine the branching ratios of exclusive channels.

In a BESII physics analysis, an estimate was made of the branching ratio uncertainty for an inclusive process ($\psi(2S) \rightarrow 4$ prongs) due to the run-to-run beam energy fluctuations [33]; it was at the level of 0.23%. Such an uncertainty is negligible when the statistical and systematic uncertainties are at the level of 10%. However, for BESIII

physics analyses, the branching ratio errors may be around 1% - 2%, and uncertainties of 0.23% can not be neglected. For exclusive processes, the branching ratio uncertainties due to beam energy errors can be much greater. As an example, in the analysis of $\psi(2S) \rightarrow \tau^+\tau^-$, this uncertainty was 5% [34]. Here, once more, it is extremely important to determine the beam energy precisely in order to be able to measure branching ratios with high precision.

7 New beam energy measurement technique

Above the importance of measuring the beam energies at BESIII has been emphasized. Luckily, a new technique, using Compton backscattering from a monochromatic laser beam incident on an electron beam, has been developed and used at Novosibirsk in the BESSY-I and BESSY-II [35] and VEPP-4M and VEPP-3 [36] storage rings. It can be used to determine the absolute energy with an accuracy at the level of $\Delta\varepsilon/\varepsilon \sim 10^{-5}$. Such a technique is especially needed at BEPCII.

The general idea is based on the following:

- The maximum energy of the back scattered photons ω_{max} (see Fig. 6) is related with the electron energy ε by the kinematics of Compton scattering:

$$\omega_{max} = \frac{\varepsilon^2}{\varepsilon + m_e^2/4\omega_0},$$

where ω_0 is the laser photon energy. If one measures ω_{max} , then the electron energy can be calculated:

$$\varepsilon = \frac{\omega_{max}}{2} \left[1 + \sqrt{1 + \frac{m_e^2}{\omega_0\omega_{max}}} \right].$$

- The very high resolution of commercially available High Purity Germanium (HPGe) detectors allows the statistical accuracy in the beam energy measurement to be at the level of $\delta\varepsilon/\varepsilon \simeq (1 - 2) \cdot 10^{-5}$.
- The systematic accuracy is mostly defined by absolute calibration of the detector energy scale. Accurate calibration can be performed in the photon energy range up to 10 MeV using γ -active radionuclides.

The measurement procedure is as follows. The laser light is put in collision with the electron or positron beam, and the energy of the backscattered photons is precisely measured using a High Purity Germanium detector (HPGe) with very high energy resolution. The maximal energy of the scattered photons is determined from the abrupt edge in the energy spectrum. Using monochromatic laser radiation as a source of initial photons with $\omega_0 \simeq 0.12$ eV, the energy of the scattered photons ω_{max} is in the range 1 - 10 MeV.

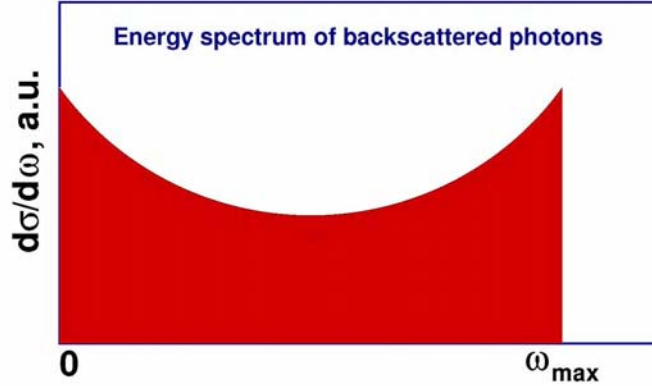


Figure 6: Energy spectrum of backscattered Compton photons. The sharp edge on the right can be used to determine the beam energy very precisely.

Figure 7 shows the relation between the measured ω_{max} and the beam energy ε . The detector energy scale can be accurately calibrated in this energy range by using well-known radiative sources of γ -radiation (Fig. 7).

The accuracy of the method has been tested by comparing it with the resonant depolarization technique in experiments at the VEPP-4M collider [37, 38]. These tests show that the two methods agree with an accuracy $\Delta\varepsilon = 40$ keV, or $\Delta\varepsilon/\varepsilon \approx 2 \cdot 10^{-5}$.

A very detailed description of the approach may be found in Ref. [39]. Below we summarize some of the formulas from this work.

7.1 Compton Scattering

The total cross section for head-on Compton scattering on an unpolarized electron is given by:

$$\sigma_c = \frac{2\sigma_o}{\lambda} \left\{ \left[1 - \frac{4}{\lambda} - \frac{8}{\lambda^2} \right] \ln(1 + \lambda) + \frac{1}{2} \left[1 - \frac{1}{(1 + \lambda)^2} \right] + \frac{8}{\lambda} \right\}, \quad (6)$$

where $\lambda = \frac{4\omega_0\varepsilon}{m_e^2}$ and where $\sigma_o = \pi \cdot r_e^2$ and r_e is a classical electron radius. If $\lambda \ll 1$ the cross section is equal to

$$\sigma_c = \frac{8}{3} \pi r_e^2 (1 - \lambda). \quad (7)$$

The energy spectrum of scattered photons for head-on Compton scattering is:

$$\frac{d\sigma_c}{dy} = \frac{2\sigma_o}{\lambda} \left\{ \frac{1}{1-y} + 1 - y - \frac{4y}{\lambda(1-y)} + \frac{4y^2}{\lambda^2(1-y)^2} \right\}, \quad (8)$$

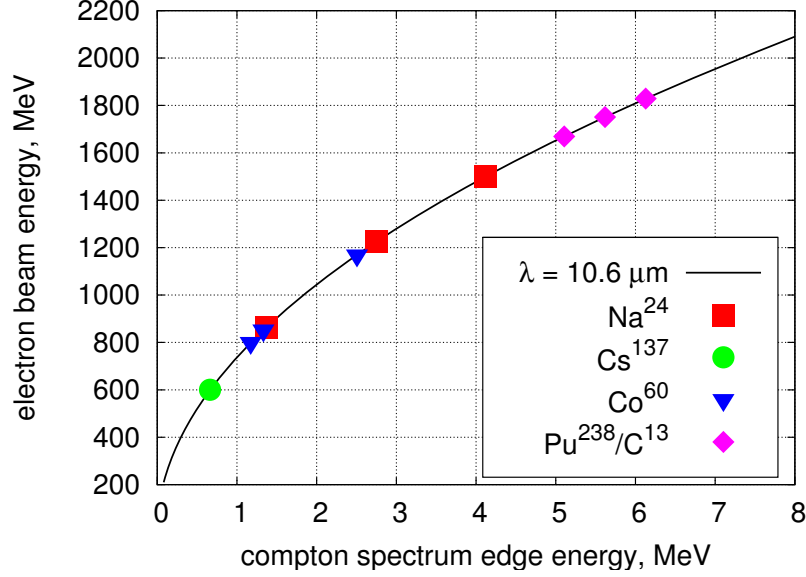


Figure 7: Relation between ω_{max} and ε (solid line). The circles, squares, triangles, and diamonds correspond to energies of γ -active radionuclides (reference lines for the HPGe detector calibration).

where $y = \omega/\varepsilon$ and ω is the energy of the scattered photon.

7.2 Beam energy measurement

The maximum photon energy ω_{max} is measured by fitting the energy spectrum edge (see Fig. 8) with the function:

$$g(x, p_{0...5}) = \frac{1}{2}(p_4(x - p_0) + p_2) \times \operatorname{erfc} \left[\frac{x - p_0}{\sqrt{2}p_1} \right] - \frac{p_1 p_4}{\sqrt{2\pi}} \times \exp \left[-\frac{(x - p_0)^2}{2p_1^2} \right] + p_5(x - p_0) + p_3, \quad (9)$$

where p_0 is the edge position, p_1 is the edge width, p_2 is the edge amplitude, p_3 is a background parameter, and p_4 and p_5 describe slopes on the right and left from the edge.

Under the actual experimental conditions the abrupt edge of the scattered photons energy distribution (Fig. 8) is smeared due to the following effects:

- the energy spread in the electron beam $\delta\varepsilon/\varepsilon$,
- the width of laser radiation line $\delta\omega_0/\omega_0$,
- the energy resolution of the HPGe detector $\delta R/R$,

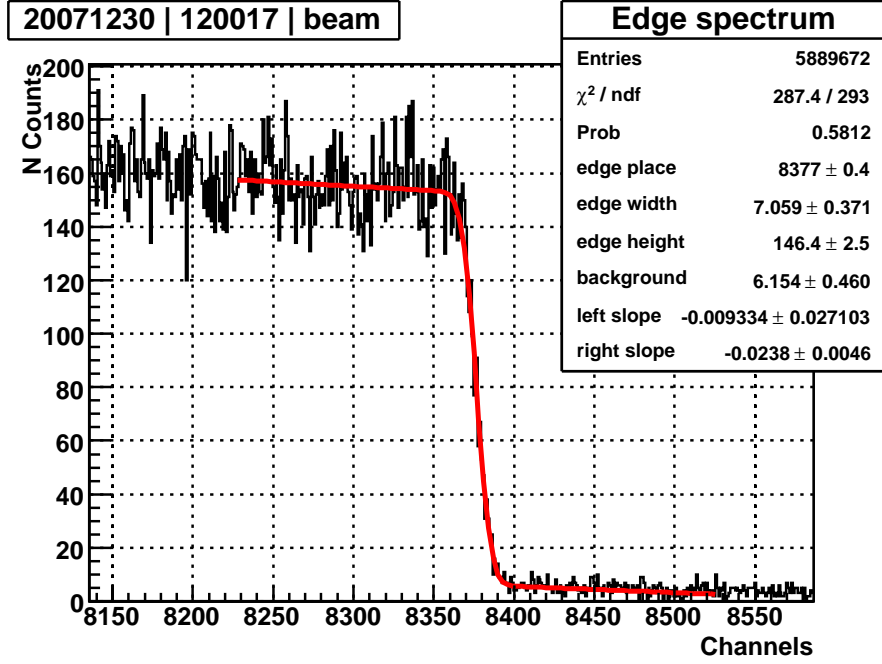


Figure 8: Shown is the energy spectrum of back scattered photons from the VEPP-4M experiment, obtained on December 30, 2007 after 30 minutes of data taking. The line is the fit result.

- the angular distribution between initial particles.

Taking into account these contributions the visible edge width can be written as

$$\sigma_\omega \equiv \frac{\delta\omega_{max}}{\omega_{max}} \simeq 2 \frac{\delta\varepsilon}{\varepsilon} \oplus \frac{\delta\omega_0}{\omega_0} \oplus \frac{\delta R}{R} \oplus \frac{\delta\alpha}{\tan \frac{\alpha}{2}}, \quad (10)$$

where $\alpha \sim \pi$ is the angle between the initial electron and the initial photon momentum, and $\delta\alpha \simeq \sigma'_e \oplus \sigma'_l$ is the sum of the electron and laser beams angular spreads added in quadrature. This contribution is negligible when $\alpha \simeq \pi$.

The relative accuracy of the ε measurement is

$$\frac{\Delta\varepsilon}{\varepsilon} \simeq \frac{1}{2} \frac{\Delta\alpha}{\tan(\alpha/2)} \oplus \frac{1}{2} \frac{\Delta\omega_0}{\omega_0} \oplus \frac{1}{2} \frac{\Delta\omega_{max}}{\omega_{max}}. \quad (11)$$

Here the contribution due to the angle α uncertainty can be omitted also. The contribution of the laser photon energy stability is negligible $\Delta\omega_0/\omega_0 < \sim 10^{-7}$. The last term is the energy measurement accuracy of the backscattered photons. It depends on the width of the spectrum edge, the number of events, and the accuracy of the HPGe detector

absolute calibration. The statistical accuracy of the ω_{max} determination can be estimated as follows:

$$\Delta\omega_{max} \simeq \sqrt{\frac{2\delta\omega_{max}}{\frac{dN_\gamma}{d\omega}(\omega_{max})}}, \quad (12)$$

where $\delta\omega_{max}$ is the edge width (Eq. (10)) and $\frac{dN_\gamma}{d\omega}(\omega_{max})$ is the photon density at the spectrum edge. The density can be estimated as:

$$\frac{dN_\gamma}{d\omega}(\omega_{max}) = \epsilon \cdot L_{e\gamma} \cdot t \cdot \frac{d\sigma_c}{d\omega}(\omega_{max}), \quad (13)$$

where $\frac{d\sigma_c}{d\omega}(\omega_{max})$ is the Compton cross section at the edge (Eq. (8)), ϵ is the photon detection efficiency, $L_{e\gamma}$ is the photon-electron luminosity, and t is the spectrum accumulation time.

7.3 Laser - electron luminosity

The electron-photon luminosity $L_{e\gamma}$ determines the number of scattered photons per electron bunch:

$$N_\gamma = L_{e\gamma} \cdot \sigma_c(\omega_0, \varepsilon), \quad (14)$$

where $\sigma_c(\omega_0, \varepsilon)$ is the total cross section of Compton scattering. The luminosity $L_{e\gamma}$ depends on the intensity of the electron and photon beams and their effective cross section.

The laser light propagation can be considered in the framework of the Gaussian beam optics approach. By definition, the transverse profile of the intensity of the Gaussian beam with a power P can be described with a function [40]:

$$I(r, s) = \frac{P}{\pi w(s)^2/2} \exp\left\{-2\frac{r^2}{w(s)^2}\right\}, \quad (15)$$

where r is the distance from the beam axis, the beam radius $w(s)$ is the distance from the beam axis where the intensity drops to the level of $1/e^2$, and s is the distance along the beam direction from the laser. The laser beam transverse photon density is written as

$$\rho_{ph}(x, y, s) = \frac{n_{ph}}{2\pi\sigma(s)^2} \exp\left\{-\frac{x^2}{2\sigma(s)^2} - \frac{y^2}{2\sigma(s)^2}\right\}, \quad (16)$$

where $\sigma(s) \equiv \frac{1}{2}w(s)$ and n_{ph} is the longitudinal density of laser photons. For any laser, operating in CW mode:

$$n_{ph} = \frac{dN_{ph}}{ds} = \frac{P}{\omega_0 c e} \equiv \frac{P\lambda}{hc^2}, \quad (17)$$

where P is the CW laser power, ω_0 is the laser photon energy, λ is the laser radiation wavelength.

The electron beam parameters are:

- N_e – number of particles in a bunch
- $\sigma_x(s) = \sqrt{\epsilon_x \beta_x(s)}$ – horizontal betatron size
- $\sigma_y(s) = \sqrt{\epsilon_y \beta_y(s)}$ – vertical betatron size
- σ_e – longitudinal electron beam size
- σ_ε – beam energy spread
- $\varepsilon, \varepsilon_0$ – particle energy and average particle energy
- $(\varepsilon - \varepsilon_0)/\varepsilon_0 \cdot \psi(s)$ – shift in x due to dispersion function ψ
- $\sigma_\psi = \psi \cdot (\sigma_\varepsilon/\varepsilon_0)$ is the part of the transverse horizontal electron beam size, which originates from non-zero dispersion function ψ .

The electron beam distribution can be written as follows:

$$\rho_e(x, y, \varepsilon, s) = \frac{N_e}{(2\pi)^{3/2} \sigma_x \sigma_y \sigma_\varepsilon} \times \exp\left\{ -\frac{(\varepsilon - \varepsilon_0)^2}{2\sigma_\varepsilon^2} - \frac{(y - y_0)^2}{2\sigma_y^2} - \frac{(x - x_0 - \psi \frac{\varepsilon - \varepsilon_0}{\varepsilon_0})^2}{2\sigma_x^2} \right\}. \quad (18)$$

Here x_0 and y_0 depends on s and indicate the possible bias between the axes of the electron and laser beams. This shift can be a result of the beams improper alignment or non-zero crossing angle.

The luminosity integrated over x , y , and ε is

$$\frac{dL_{e\gamma}}{ds} = \frac{n_{ph} N_e}{\pi \sqrt{(\sigma^2 + \sigma_x^2 + \sigma_\psi^2)(\sigma^2 + \sigma_y^2)}} \times \exp\left\{ -\frac{y_0^2}{2(\sigma^2 + \sigma_y^2)} \right\} \times \exp\left\{ -\frac{x_0^2}{2(\sigma^2 + \sigma_x^2 + \sigma_\psi^2)} \right\}. \quad (19)$$

The integration of Eq. (19) over s (formal limits of integration are defined by \mathcal{L} , which is the length of the interaction region of the two beams) can be performed numerically, using the actual sizes of the electron and laser beams.

8 Energy measurement at BESIII

Absolute energy calibration plays a crucial role in the τ mass measurement and elsewhere. A technique based on Compton backscattering is proposed for BESIII to directly measure the beam energy accurately.

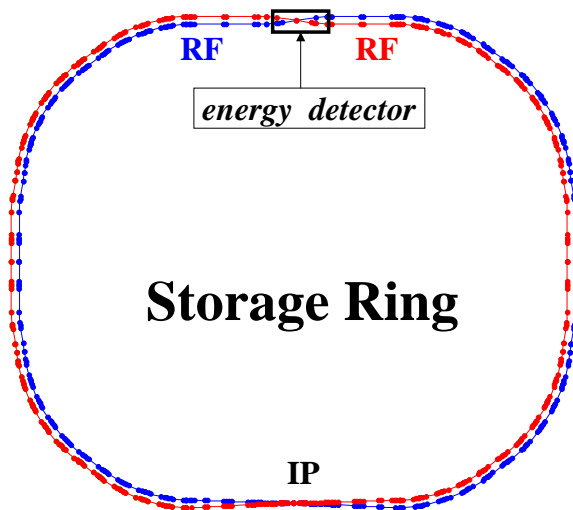


Figure 9: Location of the energy measurement system at BESIII.

The beam energy measurement system will be located at the north interaction point (IP) of the storage ring, as shown in Fig. 9 (labeled as energy detector). The layout schematic of the system is shown in Fig. 10. This design allows us to measure the energies of both the electron and positron beams with one laser and one HPGe detector. It is composed of the following parts:

1. Laser source.
2. Optics to transport the laser beam into the interaction region where the laser beam collides with either the electron or positron beam.
3. High purity Germanium detector (HPGe) to measure backscattered high energy γ -rays or X -rays.

In the following, we describe each system. Finally, the energy measured at the north IP must be corrected for synchrotron radiation loss between the north and south IPs. This is approximately 200 keV, and the corresponding error is less than 10% or 20 keV.

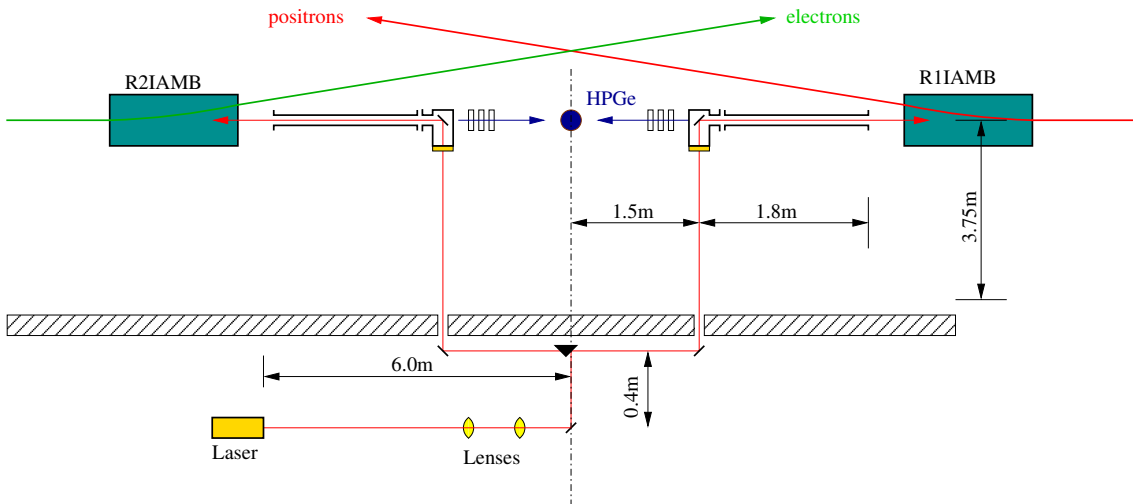


Figure 10: Simplified schematic of the energy measurement system. The positron and electron beams are indicated. R1IAMB and R2IAMB are accelerator magnets, and the high purity Germanium detector (HPGe) detector is represented by the dot at the center. The shielding wall of the beam tunnel is shown cross-hatched, and the laser will be located outside the tunnel.

8.1 Laser source and power meter

The laser will be located outside the beam tunnel, as shown in Fig. 10. A continuous operation (CW), high power, and single-line narrow-width laser is required for this application. An excellent candidate is the GEM Select Ultra-Stability 50 CO₂ laser with a fixed grating from Coherent, Inc [41]. It is compact, lightweight, and rugged with outstanding beam quality and stability, and it has adjustable power output and provides 25 – 50 W of CW power at the wavelength 10.591 μm . The average energy stability is about 0.1 ppm. It has autonomous frequency/amplitude control, which locks the output wavelength to the center of the rotational line profile, and an internal visible laser pointer to allow easy alignment. A laser of this type has been used in a similar system at the VEPP-4M collider at Novosibirsk since 2005. During this period no degradation of its parameters was noticed. The laser consumes about 1 kW of power and requires a cooling system. It is permanently sealed with no gas consumption. We will purchase the cooling system and DC power supply along with the laser. A drawing of the laser head is shown in Fig. 11, and its specifications are listed in Table 3.

The line structure of the laser is shown in Fig. 12. A CO₂ laser can radiate photons spontaneously from several lines simultaneously. For our application, we will select a single line at 10.591 or 10.611 μm , which gives a back-scattered Compton photon in the desired energy range. The width of a line is formed by Doppler and collision widening, resulting in about 100 MHz bandwidth ($\Delta\nu/\nu \simeq 3$ ppm).

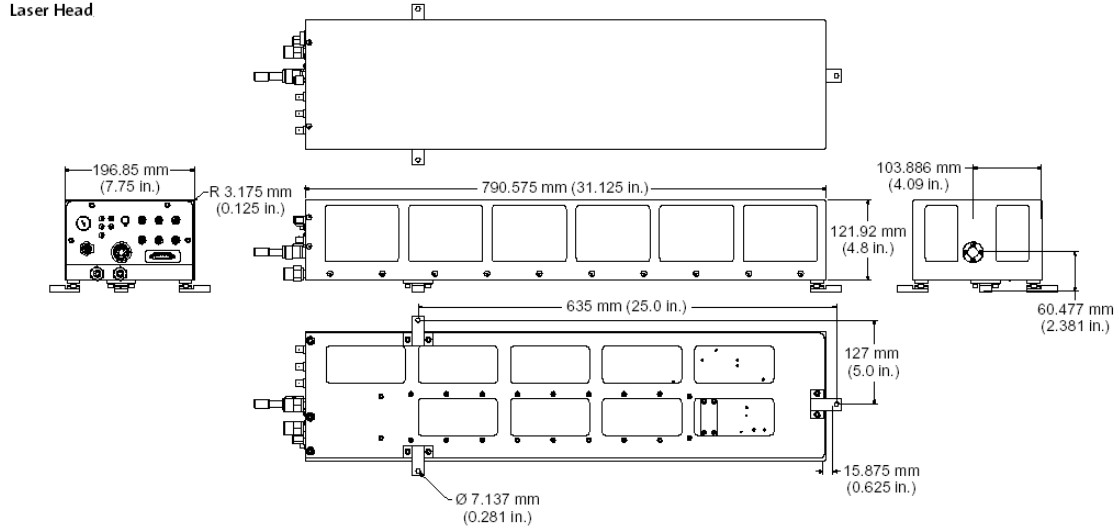


Figure 11: Dimensions of GEM Select 50 laser head.

Table 3: GEM Select 50 Specifications. ^a Dow Frost is a trademark of the Dow Chemical Company.

Output Power (W)	> 50
Wavelength (μm)	10.6 nominal
Mode Quality	TEM ₀₀
Polarization	Fixed Linear
Beam Diameter (mm, $1/e^2$)	1.7 ± 0.2
Beam Divergence (mrad)	8.3 ± 0.6
Power Stability (%)	$\pm 3\%$
Electrical	200 to 240 VAC, 50 to 60 Hz, < 8 A
Cooling	Water + 25% Dow Frost ^a 1.5 GPM/(20 ⁰ \pm 5 ⁰)C
Weight (Laser Head)	18.14 kg
Dimensions (LxWxH)	791 x 197 x 171 mm

Averaging the radiation wavelength over longitudinal cavity modes results in average laser photon energy stability at the level of $\Delta\nu/\nu < \sim 0.1$ ppm. Thus the single-line carbon dioxide laser is an excellent radiation source for the calibration system.

In order to measure the time variation of the laser performance and power losses along the optical path, we will also acquire a Coherent Field MaxII-TOP Power Meter with a PM150-50 air cooled thermopile sensor. The meter features a PC host interface, LabView drivers, analogue output, and expanded pyroelectric sensor capability. Together with the

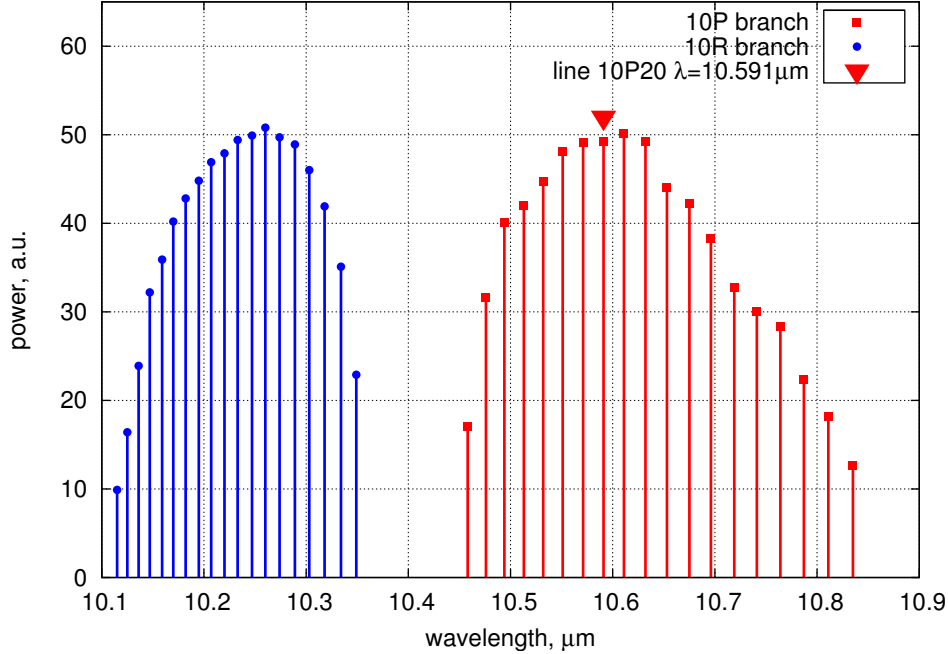


Figure 12: Transition lines of the CO_2 molecule. Either the 10.591 or the 10.611 μm line will be selected.

appropriate sensor, the FieldMaxII can measure UV, visible, and IR laser output from the nanowatt to the kilowatt range, and work with CW and pulsed lasers. The meter is ideal both for field applications and general laboratory use. The sensor is 150 mm diameter x 118 mm deep with a 50 mm aperture and can handle 150W continuously.

8.2 Optics

As shown schematically in Fig. 10, the laser beam is focused using a doublet of lenses, reflected through an angle of 90° using a 45° mirror, and then reflected either to the right or left by means of a movable prism. The beam is again reflected by 90° through a hole in the wall of the beam tunnel and is then incident on a window in a vacuum pipe extension of the beam pipe. After being reflected once more through 90° , the laser beam collides with the charged particle beam in a region upstream of either the R1IAMB or R2IAMB bending magnets.

The optical components require careful alignment and mechanical stability. It is very convenient to have free access to them independent of collider operation. These elements will be placed outside the BEPC-II tunnel, as shown in Fig. 10. The following optical units are situated along the collider tunnel wall:

1. two lenses with focal lengths of $f = 40$ cm and the laser,

2. a movable reflector prism which allows the laser beam to be directed towards the e^+ or the e^- beam pipe,
3. two mirrors to reflect the right- or left-traveling laser beam into the beam tunnel. The mirrors are installed on special supports that allow precise vertical and horizontal angular alignment by the use of stepping motors (one step equals to 1.5×10^{-6} rad).

The real life optical components, which were installed in May 2008, are shown in Fig. 13, and a closeup is shown in Fig. 14. The real life situation is somewhat different than the schematic. The laser beam after the lens doublet is bent vertically rather than horizontally. It then strikes the prism, where it is reflected left or right, depending on the position of the prism. The beam is then bent 45° into holes in the tunnel wall as described above. Fig. 15 shows the individual components installed in the system.

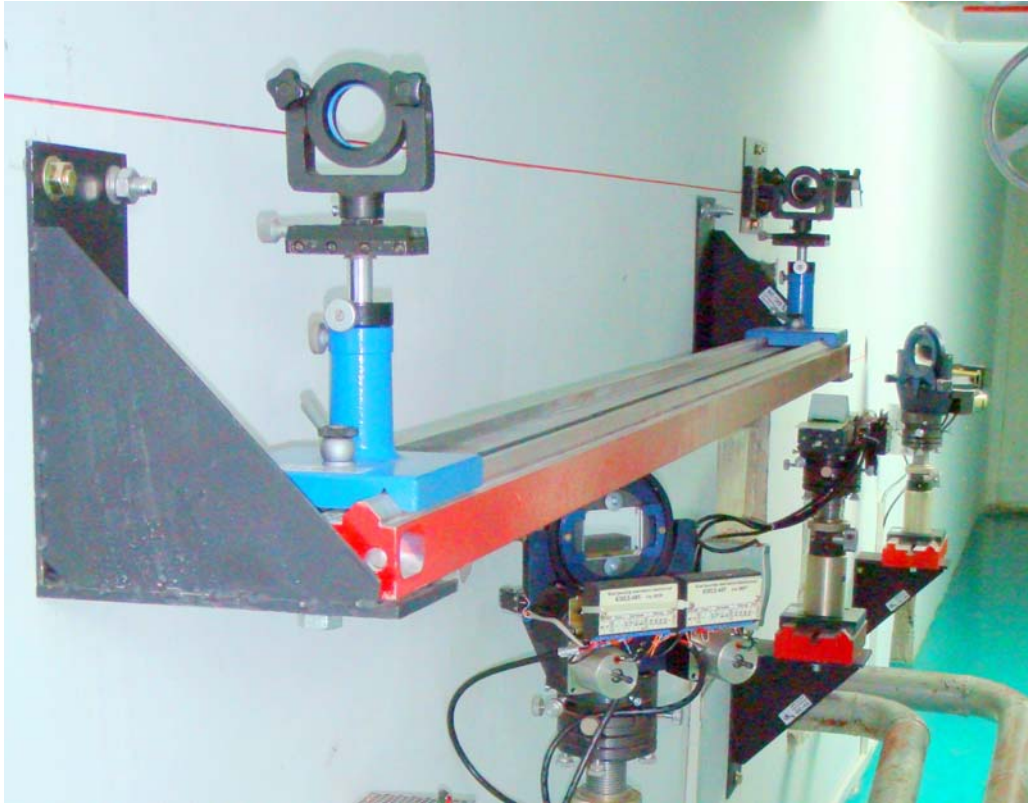


Figure 13: Optical components. Shown are the lens doublet, the 45° mirror that reflects the beam vertically, the movable prism, and two 45° mirrors that reflect the beams through holes in the tunnel wall.

The total distance from the laser output aperture to the entrance flange of the BEPC-II vacuum chamber is about 13.5 m. The laser beam traverse size at this flange should



Figure 14: A closeup of the optical system, showing the second lens of the lens doublet, the 45° mirror that reflects the beam vertically, and the movable prism.

be equal to 0.20 - 0.25 cm (see Figs. 20 and 21). The lenses should be placed 300.0 and 381.6 cm from the laser in order to provide this size (Fig. 16).

8.3 Laser-to-vacuum insertion

One of the most difficult parts of this scheme is the insertion of the laser beam into the vacuum chamber. The conceptual scheme for the laser-to-vacuum insertion system is shown in Fig. 17. A ZnSe or ZnS (Cleartran®) entrance window is used. In the vacuum chamber the laser beam is reflected through an angle of 90° by a copper mirror, which is mounted with a good thermal contact on a massive copper support. This support can be turned by bending the vacuum flexible bellow, so the angle between the mirror and the laser beam can be adjusted as necessary. After backscattering the photons return to the mirror, pass through it, leave the vacuum chamber, and are detected by the HPGe detector.

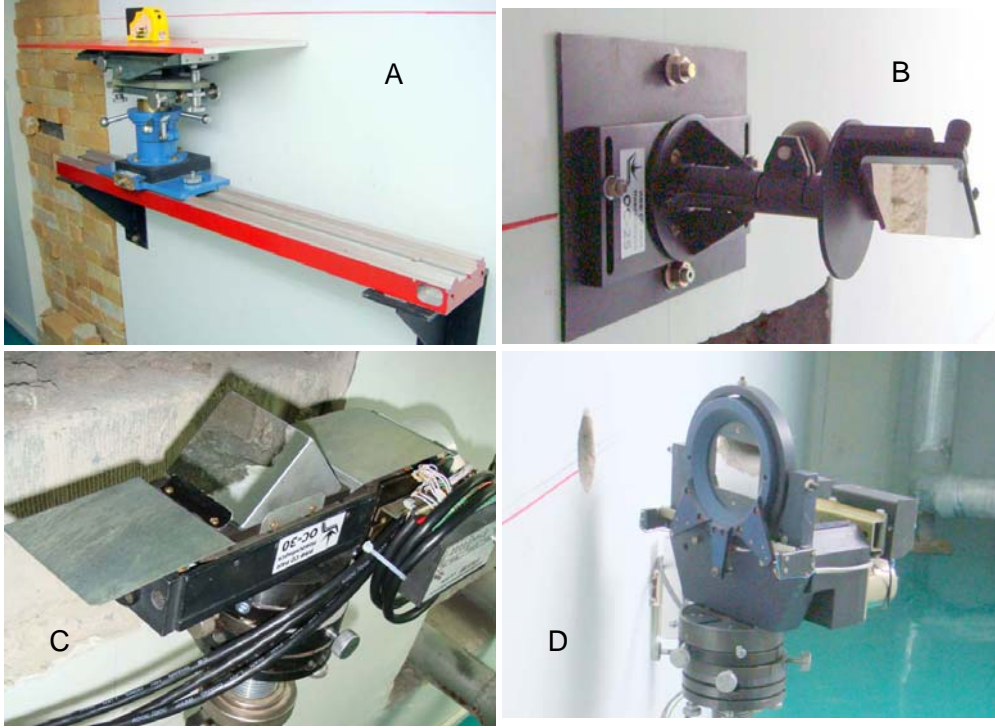


Figure 15: Optical components: A.) Shelf for CO_2 laser. B.) Mirror that reflects the beam vertically. C.) Movable prism. D.) One of the mirrors that reflects the beam through a hole in the tunnel wall.

Synchrotron radiation photons also fall on the mirror and heat it. In order to reduce the heating of the mirror, it is placed 1.80 m from the BEPC-II vacuum chamber flange. The synchrotron radiation (SR) power absorbed by the mirror can be estimated as follows:

$$P \text{ [W]} = U_0 \text{ [eV]} \cdot I \text{ [A]} \cdot \frac{\phi}{2\pi}, \quad (20)$$

where I is the beam current, U_0 is the particle energy loss per turn due to SR radiation, $\phi \simeq D/L$. Here $D \simeq l/\sqrt{2}$ is the mirror size seen from the SR photons radiation point (l is the mirror width), L is the distance between the mirror and the SR photons radiation point. The energy loss U_0 can be obtained using the following formula:

$$U_0 = \frac{4\pi}{3} \cdot \alpha \cdot \hbar c \cdot \frac{\gamma^4}{\rho}, \quad (21)$$

where ρ is the beam trajectory radius in the bending magnet. Using the values of BEPC-II parameters listed in Table 4, $P = 200 \text{ W}$ is obtained. The extraction of heat to some

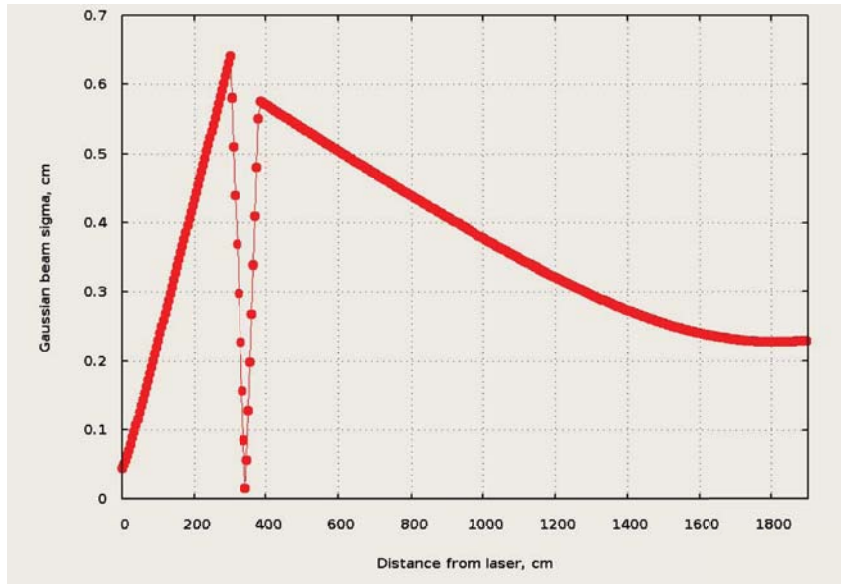


Figure 16: The laser beam transverse size versus the distance from the laser (at the origin) along the optical axis. The lenses are placed at 300.0 and 381.6 cm from the laser; the entrance flange of the BEPC-II vacuum chambers is at the distance of about 13.5 m from the laser.

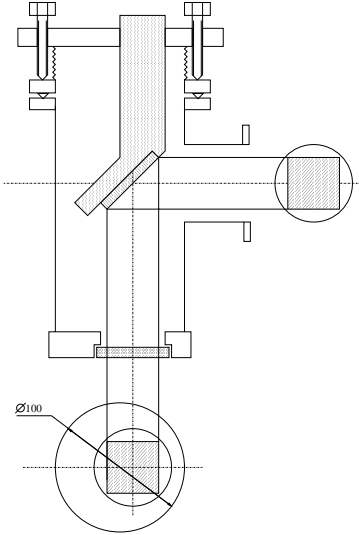


Figure 17: Laser-to-vacuum insertion assembly.

cooling system outside the vacuum chamber is provided by the massive copper support of the mirror.

The design of the BEPC-II vacuum chamber is shown in Fig. 18. The laser beam

Beam energy E , GeV	2
Beam current I , A	0.91
Bending radius ρ , cm	913
Mirror size D , cm	4.0
Distance to mirror $L = L_1 + L_2$, cm	460 = 280 + 180
$\phi \simeq D/L$, mrad	8.7
SR power on the mirror, W	200

Table 4: The parameters necessary for calculation of the SR power. L_1 is the distance from SR photons radiation point to the BEPC-II vacuum chamber flange, L_2 is the distance from the BEPC-II vacuum chamber flange to the mirror.

insertion system is connected to the flange of the chamber. The distance between the vacuum chambers flanges of the electron and positron rings is 6.6 m. The HPGe detector is placed half way between the flanges (Fig. 10).

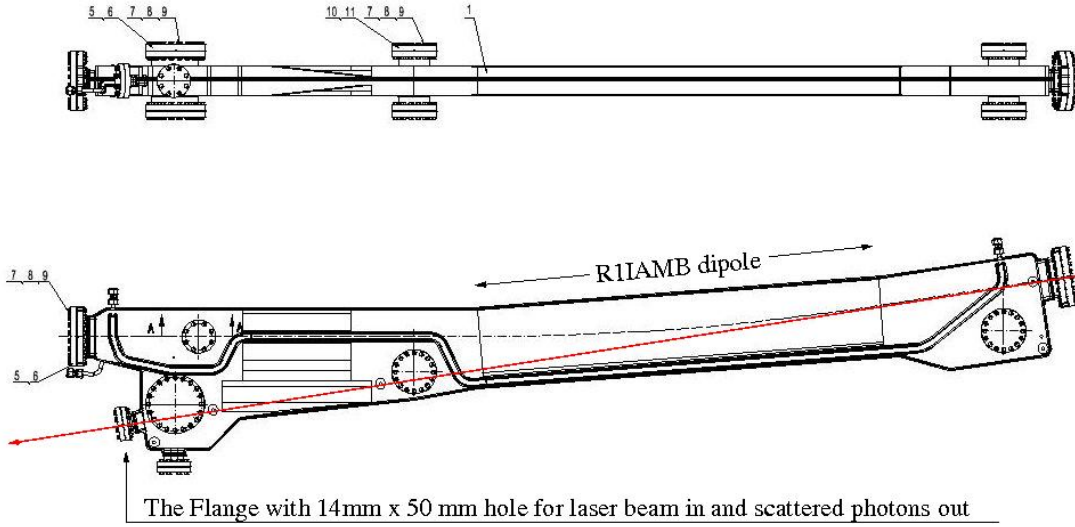


Figure 18: BEPC-II vacuum chamber.

8.4 Compton backscattering region

The laser and e^-/e^+ beams will interact in the straight sections of BEPC-II, between the R1IMB01 and R1IAMB dipoles for e^+ (R2IMB01 and R2IAMB for e^-). The lattice functions of the BEPC-II straight section are shown in Fig. 19. The electron and laser beam size in x and y projections versus z -coordinate of the beam axis are shown in

Figs. 20 and 21. The laser beam is focused at the BEPC-II vacuum chamber entrance flange, where the geometrical aperture is minimal (vertical size is 14 mm).

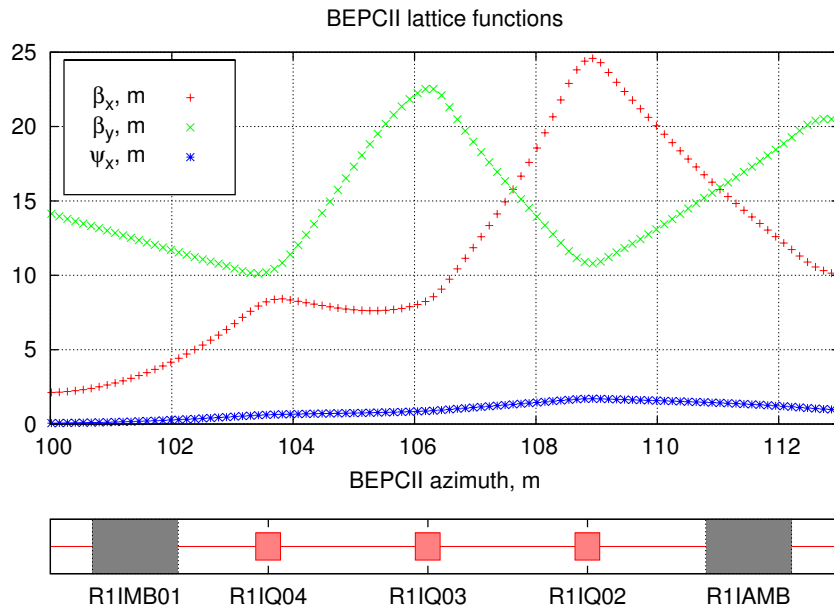


Figure 19: BEPC-II lattice functions in the interaction area versus beam coordinate z . The positions of collider magnets are shown at the bottom of the picture.

The scattered photon flux (Fig. 22) is calculated numerically using the following formula:

$$\frac{dN_\gamma}{ds} = \frac{dL_{e\gamma}}{ds} \cdot \sigma_c. \quad (22)$$

The total yield of photons is about 17000 ph/s/mA/W

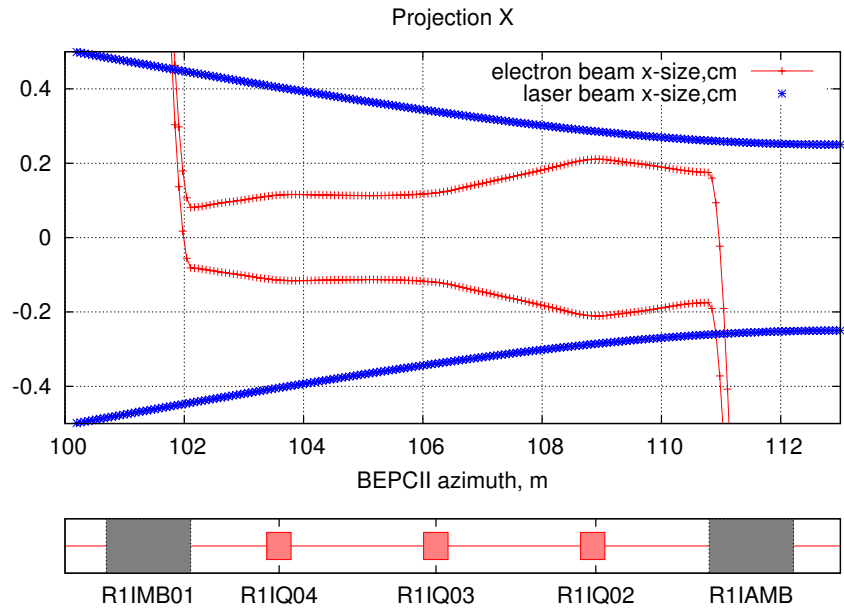


Figure 20: Laser and e^- or e^+ beam sizes ($\pm\sigma$) in the horizontal plane versus z .

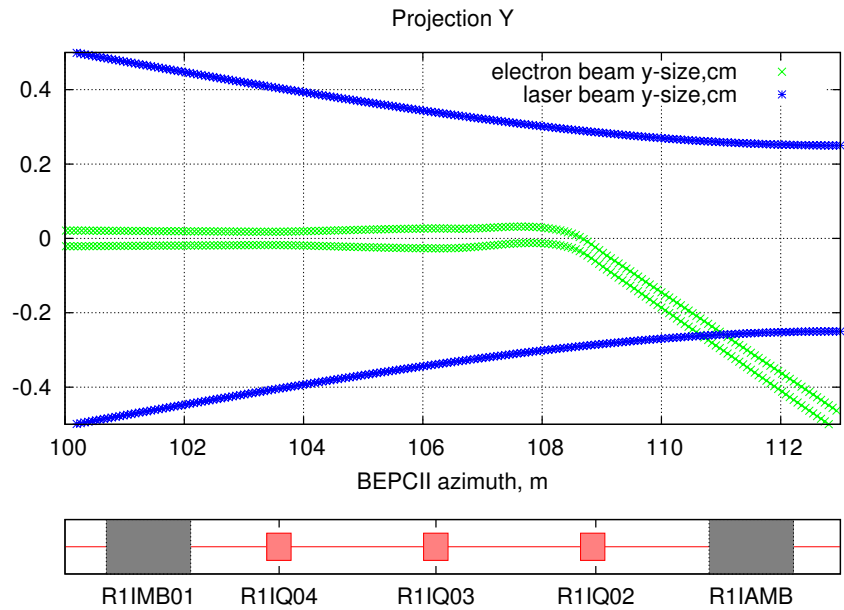


Figure 21: The Laser and e^- or e^+ beam sizes ($\pm\sigma$) in the vertical plane versus z . The vertical bending for the e^- and e^+ beams have the opposite sign.

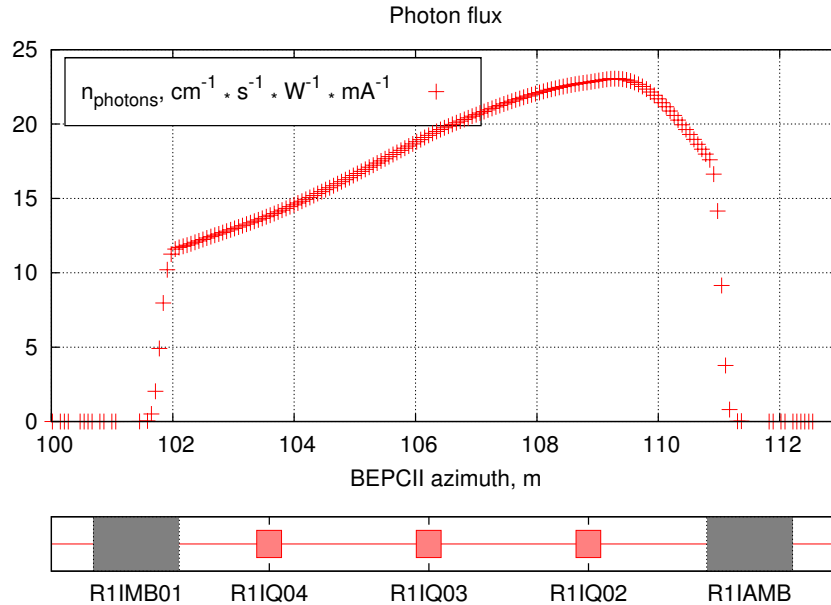


Figure 22: The flux of scattered photons versus z . The beam energy is $\varepsilon = 1890$ MeV, beam current $I_e = 1$ mA, laser power $P = 1$ W. The positions of collider magnets are shown at the bottom of the picture.

8.5 HPGe detector

The purpose of a HPGe detector is to convert gamma rays into electrical impulses which can be used with suitable signal processing, to determine their energy and intensity.

A HPGe detector is a large germanium diode of the p-n or p-i-n type operated in the reverse bias mode. At a suitable operating temperature (normally $\simeq 85$ K), the barrier created at the junction reduces the leakage current to acceptably low values. Thus an electric field can be applied that is sufficient to collect the charge carriers liberated by ionizing radiation.

The most suitable HPGe detectors for 1–10 MeV photons are Coaxial type detectors, which are hollowed out cylinders of germanium, as shown in Fig. 23. They have different volumes, and hence, different registration efficiencies. The efficiency of each detector is usually specified by a parameter called *relative detection efficiency*. The *relative detection efficiency* of coaxial germanium detectors is defined at 1.33 MeV relative to that of a standard 3-in.-diameter, 3-in.-long NaI(Tl) scintillator.

The backscattered photons will be detected in a coaxial HPGe detector manufactured by ORTEC (model GEM25P4-70) [42], which is shown in Fig. 24. GEM series germanium (HPGe) detectors are manufactured with ORTEC’s own germanium and represent the state of the art. Because of the superior quality of ORTEC’s germanium material, GEM detectors feature the best available energy resolution and peak symmetry at 1.33 MeV.

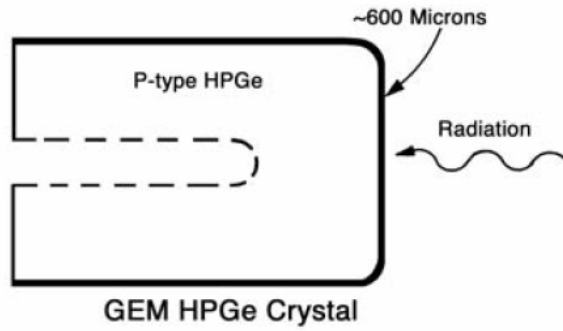


Figure 23: Schematic of HPGe detector.



Figure 24: ORTEC HPGe detector mounted on cryostat.

The energy resolution and peak symmetry are warranted to two decimal places. It has a diameter of 57.8 mm and a height of 52.7 mm with 31.2% relative efficiency at 1.33 MeV. The energy resolution for the 1.33 MeV line of ^{60}Co is 1.74 keV.

The signal processor is the Advanced Digital Gamma-Ray Spectrometer for HPGe systems, DSPEC-Pro [43], which includes hardware and software, and the preamp is A257P. The detector is connected to the spectrometric station, which transfers data using the USB port of the computer, as shown in Fig. 25.

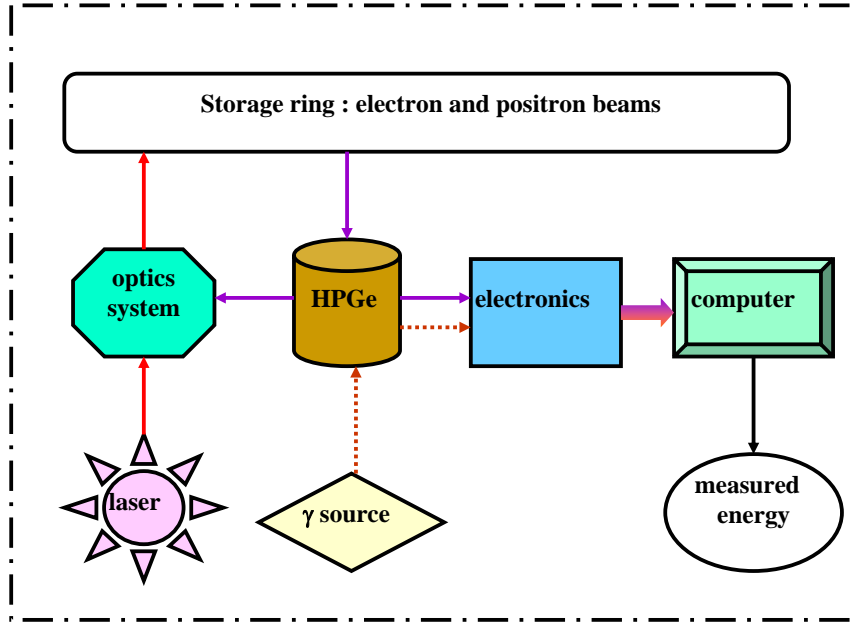


Figure 25: HPGe detector connected to electronics and readout computer.

9 Accuracy of the BEPC-II beam energy calibration system

Here we consider statistical and systematic errors of the BEPC-II Beam Energy Calibration System. This system is under construction now and will provide precise average beam energy measurement at the second interaction point of the BEPC-II collider.

9.1 Statistical Errors

9.1.1 The Compton Edge

In section 8.4, the laser-electron interaction was found to produce a lot of backscattered photons (more than $10^7 s^{-1}$ at 100 mA beam current and 10 W laser power). The HPGe detector with its signal processor will not be able to work with such a high flux of photons, so the flux will be reduced until the counting rate of the detector will be about $10^4 s^{-1}$. This attenuation will be performed by using a larger laser beam size and by placing absorbers between the photon beam and the detector. So the situation will be similar to that at the VEPP-4M collider, where the beam energy range and the energy spread are almost the same as for BEPC-II. The statistical contribution to the error is $\Delta E/E \simeq 3 - 5 \cdot 10^{-5}$ for a 15 min spectrum accumulation time.

9.1.2 The Energy Scale

The detector energy scale calibration will be performed by measuring radio-nuclide lines for every spectrum recorded, and this will provide additional errors of a statistic nature. This contribution may be minimized to the level $\Delta E/E \simeq 1 - 2 \cdot 10^{-5}$ by the adjustment of the corresponding counting rate, so it has almost no contribution to the final accuracy.

9.2 Systematic Errors

9.2.1 Non-linearity of the HPGe energy scale

At present this is the most significant contribution to the systematic uncertainty. At VEPP-4M the calibration was done without high-energy γ -lines (i.e. without 6.13 MeV photons and corresponding escape peaks). The contribution to the total error was $\Delta E/E \simeq 1.5 \cdot 10^{-4}$. This non-linearity was then studied and corrected to $\Delta E/E \simeq 3 \cdot 10^{-5}$ with resonant depolarization beam energy measurements. With the proper calibration source (Pu-C), we expect to have this error at the same level or even better without using resonant depolarization. This will be tested at VEPP-4M (in Autumn 2008).

9.2.2 Other sources of systematic errors

Other possible sources of systematic errors considered are:

- Non-gaussian response of the HPGe detector at high counting rates.
- Particle energy distribution in the beam – is it Gaussian as it is assumed in the edge fit function?
- Background from multiple Compton events near the edge.
- Correlations between electron angle/position in the beam and its energy.

we believe these will be negligible for the BEPC-II experiment.

10 Background measurements

The HPGe detector used in our experiment will be located near the vacuum pipes of the electron and positron beams at BEPCII. Since HPGe is highly sensitive, the radiation environment is crucial for the proper performance of the detector. Therefore, it is of great importance to measure the radiation dose at and around the position where the HPGe detector will be located.

Besides the safety of the HPGe detector, the safety of workers is another important reason for radiation dose measurements. According to Fig. 10, there is merely a shielding wall with thickness around 0.5 meters between the tunnel and the corridor where the optics system is located and where adjustments need to be performed. Measurements of radiation doses were performed from March, 2008 to May, 2008. The results for γ , β and neutron radiation were obtained, allowing the necessary shielding thickness for the safety of the HPGe detector to be estimated.

The radiation dosimeters used at BEPCII were provided by Landauer Inc. [44]. Two types of detector were used. The first one was an optically stimulated luminescence detector (OSLD) made of carbon-doped aluminum oxide ($Al_2O_3:C$), which is mainly used for γ , β , and X-ray detection. The second detector was a solid state nuclear track detector (SSNTDs) made of allyl diglycol carbonate ($C_{12}H_{18}O_7$), which is mainly used for neutron detection. Used in this work are IZ-type dosimeters which consist of both I-type and Z-type dosimeters. The former is an assembly of metal and plastic filters along with OSLD detectors; while the latter is composed of one SSNTD and a polyethylene radiator.

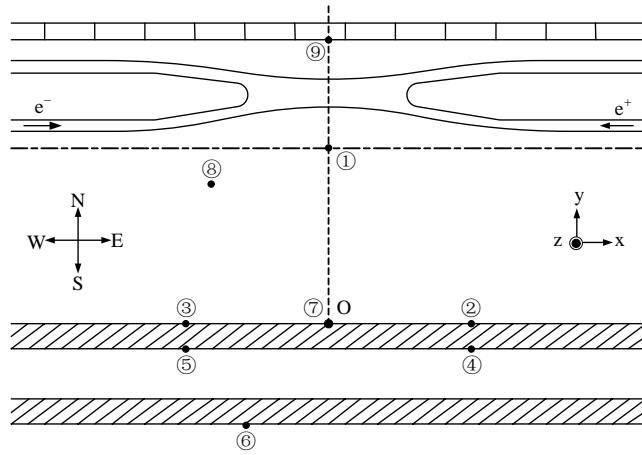


Figure 26: Top view of the BEPCII north interaction point. Two hatched bands indicate the two concrete walls with thickness 50 cm each; the top block band denotes the support for various wires and cables; and the two cross bands are the vacuum pipes for the electron and positron beams. Circled numbers indicate the positions for radiation dose measurements.

A total of fifteen IZ-type dosimeters were used in the two sets of measurements, ten in the first and five in the second. The positions of each dosimeter are shown in Fig. 26, and the detailed coordinates are listed in Table 5. The energies detected by OSLD range from 5 keV to 40 MeV for gammas and X-rays and from 150 keV to 10 MeV from β particles, while the energies detected by SSNTD range from 40 keV to 40 MeV for fast neutrons. The corresponding dose measurements range from 0.01 mSv to 10 Sv (γ and X-ray), 0.1 mSv to 10 Sv (β), and 0.2 mSv to 250 mSv (neutron). It should be noted here that the

Table 5: Results of radiation dose measurements. As shown in Fig. 26, “ O ” denotes the origin of coordinates; the positive (negative) x -axis represents the east (west) direction; the positive (negative) y -axis represents the north (south) direction; $z = 0$ denotes the ground level of the storage ring tunnel and the positive (negative) z -axis represents the upwards (downwards) direction. The dosimeter at 8 is exposed in the air while the one at 8* is shielded by a lead brick with thickness 5 cm.

Order	Position	Measured Dose	
	(x, y, z) [cm]	$\gamma&\beta$	Neutron [m Sv]
First set			
①	(0,370,120)	6.44	0.07
② 2a	(300,0,10)	1.19	0.09
2b	(300,0,120)	1.36	0.12
2c	(300,0,270)	1.15	0.14
③ 3a	(-300,0,10)	0.58	0.12
3b	(-300,0,120)	0.74	0.07
3c	(-300,0,270)	0.67	0.07
④	(300,-50,110)	0.06	0.26
⑤	(-300,-50,110)	0.03	0.05
⑥	(-180,-240,30)	0.03	0.05
Second set			
①	(0,370,120)	2.42	< 0.2
⑦ 7a	(0,0,10)	1.45	< 0.2
7b	(0,0,120)	2.47	< 0.2
⑧ 8	(-250,300,100)	1.20	< 0.2
8*	(-250,300,90)	< 0.01	< 0.2

conditions for two sets of measurements are rather different. For the first, there were both positron and electron beams with currents around 400 to 500 mA for each beam, and the measurement time was about three days. For the second, only the electron beam was present with intensity around 200 to 250 mA, and the measurement time was about 8 days.

When the measurements were finished, all dosimeters were collected and returned to Landauer for analysis. All results are tabulated in Table 5.

From Fig. 26 and Table 5, we obtain a general understanding of radiation at the north IP. Let us begin with the first measurement set for γ and β .

First, the radiation dose at ① is 6.44 mSv which is about 200 times higher than that at ⑥, 0.03 mSv, which is safe for human activity. If we want to have the same level of low radiation as point ⑥ around point ① where the HPGe detector will be located, some shielding will be needed. As an approximate estimation, the needed thickness of lead is calculated by the following formula

$$D_x = D_0 e^{-\mu x}, \text{ or } x = \frac{1}{\mu} \cdot \ln \frac{D_0}{D_x}, \quad (23)$$

where μ is the linear attenuation coefficient for the photons of the energy of interest in the shield material; x is the shield linear thickness; D_0 is the unshielded dose while D_x the shielded dose at the point of interest outside the shield. Values of μ are available in a variety of sources [45]. For our case, for $E_\gamma \approx 8$ MeV, with $D_x/D_0 \approx 200$ and $\mu = 0.55$, Eq. (23) yields $x \approx 9.63$ cm of lead.

Second, comparing the measurements of a, b, c at the position ② or ③, it can be seen that the radiation dose at b is greater than those at a and/or c which means the radiation at the level of the vacuum pipe is higher, as expected.

Third, referring to Fig. 26, it is seen that the radiation is higher on the east side (②), where the positron beam is closer to the wall than on the west side (③), where the electron beam is closer to the wall. This is consistent with expectations.

For the neutron background, the results listed in Table 5 indicate that the radiation dose at ① (0.07 mSv) is almost the same as that at ⑥ (0.05); neutron radiation at the HPGe detector is fairly small. However, the neutron dose at ④ (0.26 mSv), where the dose is expected to be smaller than that at point 2b of ② (0.12 mSv), is larger. This indicates that further detailed measurements are needed.

Qualitatively, the second measurement set results are also reasonable. The measurement results at 8 and 8* indicate that the lead shielding can greatly decrease the radiation dose of γ and β . This measurement is also qualitatively consistent with the estimation obtained by Eq. (23).

Our measurements indicate that the HPGe detector with shielding should be able to work stably and without damage at the north interaction of BEPCII. However more measurements will be taken with final beam conditions.

11 Collaboration, budget, and schedule

The development of the beam energy calibration system for the BEPC-II collider is a collaboration between the Budker Institute of Nuclear Physics (BINP) at Novosibirsk (M. N. Achasov and N. Y. Muchnoi), the Institute of High Energy Physics (IHEP) in Beijing (C. D. Fu, X. H. Mo, Q. Qin, H. M. Qu, Y. F. Wang, and J. Q. Xu), and the University of Hawaii (UH). The components of this system, their cost, and the group responsible for each component are listed in Table 6. The Budker group, besides having a great deal of expertise, are responsible for the optical components, and the HPGe detector. The IHEP group is responsible for the vacuum boxes and components, computers, and calibration sources, as well as the infrastructure for the system. UH is responsible for the laser, laser power supply, laser cooling, and a power meter. The total budget is \$356.0K, with IHEP responsible for \$142.5K, BINP for \$110K, and UH for \$103.5K. All three groups will participate in the commissioning and operation of the system. The time schedule is shown in Table 7.

12 Final budget

As described above, the development of the beam energy calibration system for the BEPC-II collider is a collaboration between the Budker Institute of Nuclear Physics at Novosibirsk, the Institute of High Energy Physics in Beijing, and the University of Hawaii (UH). UH is responsible for the laser, laser power supply, laser cooling, and a power meter. The final budget for the UH portion, shown in Table 8, includes money for travel (four trips with two trips for postdocs in training), shipping, customs, and supplies, as well as for the laser, laser power supply, laser cooling, and a power meter. Extra travel to China will be required during installation and commissioning of the beam energy measurement system.

13 Summary

The importance of the precise determination of the beam energy at BESIII has been described for many physics analyses, in particular for the precise measurement of the τ mass. Fortunately, a method has been developed by BINP physicists using back scattered Compton photons produced by CO_2 laser beams on both the electron and positron beams in BESIII. This method has been demonstrated at BESSY-I, BESSY-II, VEPP-4M, and VEPP-3 storage rings at Novosibirsk. The expected precision at BESIII is at the level of $\Delta\varepsilon = 40$ keV, or $\Delta\varepsilon/\varepsilon \approx 2 \cdot 10^{-5}$.

A collaboration has been formed between BINP, IHEP, and UH to install and commission such a system in BESIII. UH will be responsible for the CO_2 laser and a power

Table 6: Budget.

Item	Cost (\$K)	Responsibility
Design and manufacture of vacuum chamber and relevant parts:		
Vacuum boxes	36.0	IHEP
Gate valves	28.6	IHEP
Flanges	5.0	IHEP
Photon absorbers	2.5	IHEP
Ion pumps	5.8	IHEP
Penning vacuum gauges	6.0	IHEP
Optics and laser system:		
Optics and related parts	35.0	BINP
Coherent GEM Select 50 ultra-stability laser	83.7	UH
Coherent laser high stability DC power supply	9.0	UH
Coherent laser cooling system	8.0	UH
Coherent FieldMate Power Meter and PM150-50 thermopile sensor	2.8	UH
HPGe detector system:		
Ortec (GEM25P4-70) HPGe detector	75.0	BINP
Radioactive sources	10.0	IHEP
Computers (for system control)	1.5	IHEP
Other:		
Corridor modifications	4.3	IHEP
Radiation protection	35.8	IHEP
Service charge	7.0	IHEP
Total	356.0	

meter for the setup. All groups are responsible for contributing to the installation and commissioning. The total cost of the UH proposal is \$119 K.

14 Acknowledgments

We wish to acknowledge the considerable help given to us in writing this proposal by our collaborators on this project: M. N. Achasov and N. Y. Muchnoi, Budker Institute of Nuclear Physics (BINP) at Novosibirsk, and C. D. Fu, X. H. Mo, Q. Qin, H. M. Qu, Y.

Table 7: Schedule.

System Design	Oct. - Dec. 2007
Vacuum chamber design and manufacture	Jan. - Apr. 2008
Radiation background measurement	Mar. - May 2008
Install some components (mounts and optics)	May 2008
Design and produce connection part between energy measurement system and vacuum chamber	June - Oct. 2008
Test HPGe detector	June - Dec. 2008
Laser and HPGe Installation	Jan. - Mar. 2009
Complete installation and commission	Mar. - June 2009
Energy measurement	July - Aug. 2009

Table 8: Final Budget for University of Hawaii portion.

Item	Cost (\$)
Coherent GEM Select 50 Ultra-Stability Laser	83,700
Coherent High Stability DC Power Supply	8,950
Coherent Chiller for Laser	7,950
Coherent FieldMate Power Meter and PM150-50 thermopile sensor	2,800
Shipping, customs, supplies, and miscellaneous	2,000
Postdoc Travel (2 trips)	6,000
Other Travel (2 trips)	6,000
Total Direct Costs	117,400
Indirect costs	1,648
Total UH cost of project	\$ 119,048

F. Wang, and J. Q. Xu, the Institute of High Energy Physics (IHEP) in Beijing.

References

- [1] J. Z. Bai *et al.*, BES Collab., Nucl. Instrum. Meth. **A344**, 319 (1994).
- [2] J. Z. Bai *et al.*, BES Collab., Nucl. Instrum. Meth. **A458**, 627 (2001).
- [3] Preliminary Design Report of accelerator BEPCII (Second version, in Chinese; July, 2003).
- [4] C.Z. Yuan, B.Y. Zhang and Q. Qin, HEP & NP **26**, 1201 (2004).
- [5] Preliminary Design Report: The BESIII Detector, January 2004.
- [6] W.-M. Yao *et al.* (PDG), J. Phys. **G 33**, 1 (2006).
- [7] W. J. Marciano and A. Sirlin, Phys. Rev. Lett. **61**, 1815 (1988).
- [8] A. Pich, Invited talk at the XXXI International Conference on Theoretical Physics, Ustron, Poland, 5-11 Sept 2007, arXiv:0711.0028 (2007).
- [9] A. Pich, Invited talk at the International Workshop on Tau-Charm Physics, Beijing, China, June 5-7, 2006, arXiv:hep-ph/0609138 (2006).
- [10] R. Barate *et al.*, Eur. Phys. J. **C2**, 395 (1998).
- [11] J. Z. Bai *et al.*, BES Collab., Phys. Rev. **D53**, 20 (1996).
- [12] V. V. Anashin *et al.*, Nucl. Phys. Proc. Suppl. **169**, 125 (2007).
- [13] K. Abe *et al.*, Phys. Rev. Lett. **99**, 011801 (2007).
- [14] W.M. Yao *et al.* (PDG), J. Phys. **G 33**, 1 (2006), and 2007 partial update for the 2008 edition.
- [15] W. Bacino *et al.*, Phys. Rev. Lett. **41**, 13 (2007).
- [16] H. Albrecht *et al.*, ARGUS Collab., Phys. Lett. **B292**, 221 (1992).
- [17] A. Anastassov *et al.*, Phys. Rev. **D55**, 2559 (1997).
- [18] G. Abbiendi *et al.*, Phys. Lett. **B492**, 23 (2000).
- [19] Y.K. Wang, X.H. Mo, C.Z. Yuan and J.P. Liu, Nucl. Instr. Meth. **A583**, 479 (2007).
- [20] J. Z. Bai *et al.*, BES Collaboration, Phys. Rev. Lett. **69**, 3021 (1992).
- [21] J. Z. Bai *et al.*, BES Collaboration, Phys. Rev. **D 53**, 20 (1996).

- [22] M. B. Voloshin, Phys. Lett. **B 556**, 153 (2003).
- [23] J. Z. Bai *et al.*, BES Collaboration, **HEP& NP 16**, 343 (1992).
- [24] Y. K. Wang, X. H. Mo, C. Z. Yuan and J. P. Liu, **HEP& NP 31**, 325 (2007).
- [25] C. Zhang *et al.*, “Beam energy stabilization and online measurement in BEOC”, Presented at the VXth Int. Conf. on High Energy Accelerators (HEACC’92 Hamburg), Hamburg, Germany, July 20-24, 1992.
- [26] S. L. Olsen, “What’s new with the XYZ mesons?”, arXiv:0801.1153 (2008).
- [27] M. Ablikim *et al.*, BES Collaboration, Phys. Rev. Lett. **101**, 102004 (2008).
- [28] P. Wang, C. Z. Yuan and X. H. Mo: Phys. Lett. B 574, 41(2003).
- [29] P. Wang, X. H. Mo and C. Z. Yuan: Int. J. Mod. Phys. A21, 5163 (2006).
- [30] X.H.Mo and Y.S.Zhu, HEP & NP **27**, 474 (2003).
- [31] P. Wang, C. Z. Yuan and X. H. Mo, HEP & NP **27**, 456 (2003) (hep-ex/0210062).
- [32] P. Wang, X. H. Mo and C. Z. Yuan, Phys. Lett. **B557**, 192 (2003);
- [33] X.H.Mo, Y.S.Zhu, C. Z. Yuan, C. D. Fu and G. Li, HEP & NP **28**, (2004) 455-462
- [34] M. Ablikim *et al.*, BES Collaboration, Phys. Rev. **D74** (2006) 112003.
- [35] R. Klein *et al.*, Nucl. Instrum Meth A **384**, 293 (1997).
- [36] N. Muchnoi *et al.*, talk at EPAC, Edinburgh, Scotland, 26-30 June 2006, Proc. of EPAC 2006, 1181 (2006).
- [37] A.N. Skrinsky and Yu.M. Shatunov, Sov. Phys. Uspekhi 32, 548 (1989).
- [38] B.A.Shwarz for KEDR collaboration. Nucl.Phys.Proc.Suppl.169, 125 (2007). (e-Print: hep-ex/0611046).
- [39] M.N. Achasov *et al.*, “The beam energy calibration system for the BEPC-II collider”, ArXiv:0804.0159 (2008).
- [40] Encyclopedia of Laser Physics and Technology (http://www.rp-photonics.com/gaussian_beams.html).
- [41] See <http://www.coherent.com/Lasers>.
- [42] See http://www.ortec-online.com/detectors/photon/b2_1.htm.

- [43] See http://www.ortec-online.com/pdf/dsp_pro.pdf.
- [44] The detailed and comprehensive introduction about Inlight dosimeters could be found through web page:
<http://www.landauerinc.com/>
- [45] Values of μ are available at NIST (National Institute of Standards and Technology) web site:
<http://physics.nist.gov/PhysRefData/XrayMassCoef/cover.html>